Climate of the Past

Open Access

Scaling laws for perturbations in the ocean–atmosphere system following large CO$_2$ emissions

N. Towles, P. Olson, and A. Gnanadesikan

Department of Earth and Planetary Sciences, Johns Hopkins University, Baltimore, MD 21218, USA

Correspondence to: N. Towles (nathan.towles@gmail.com)

Abstract. Scaling relationships are found for perturbations to atmosphere and ocean variables from large transient CO$_2$ emissions. Using the Long-term Ocean-atmosphere-Sediment CArbon cycle Reservoir (LOSCAR) model (Zeebe et al., 2009; Zeebe, 2012b), we calculate perturbations to atmosphere temperature, total carbon, ocean temperature, total ocean carbon, pH, alkalinity, marine-sediment carbon, and carbon-13 isotope anomalies in the ocean and atmosphere resulting from idealized CO$_2$ emission events. The peak perturbations in the atmosphere and ocean variables are then fit to power law functions of the form of $\gamma D^{\alpha} E^{\beta}$, where D is the event duration, E is its total carbon emission, and γ is a coefficient. Good power law fits are obtained for most system variables for E up to 50 000 PgC and D up to 100 kyr. Although all of the peak perturbations increase with emission rate E/D, we find no evidence of emission-rate-only scaling, $\alpha + \beta = 0$. Instead, our scaling yields $\alpha + \beta \simeq 1$ for total ocean and atmosphere carbon and $0 < \alpha + \beta < 1$ for most of the other system variables.

1 Introduction

The study of how the Earth system responds to large, transient carbon emissions is of particular importance for developing a better understanding of our past, present, and future climate. Transient emissions related to the extrusion of flood basalts (10^2–10^4 PgC; McKay et al., 2014), dissociation of methane hydrates ($> 10^3$ PgC; Zachos et al., 2005; Zeebe et al., 2009), and widespread anthropogenic burning of fossil fuels ($> 10^3$ PgC; Archer et al., 2009) are a few examples.

What complicates our understanding of the response to these transient perturbations is the fact that there are many carbon reservoirs with a large range of intrinsic timescales associated with the different processes governing the Earth system. On timescales of $< 10^3$ years, exchanges between the atmosphere, biosphere, soils and ocean occur. On timescales 10^3–10^5 years, ocean carbonate–sediment interactions become significant (Archer et al., 2009). When dealing with timescales $> 10^5$ years, it becomes necessary to consider the effects of geologic processes such as silicate weathering, as these control how the system resets to a steady-state balance. The complex interactions between so many system components over such a large range of timescales make it difficult to characterize how the Earth's response to CO$_2$ perturbations of different magnitudes and durations has changed through deep time.

In general, the modeling of carbon perturbations is undertaken for two purposes. One is to predict future system changes that are expected to occur as a result of a particular emission history, such as the history of anthropogenic emissions in the industrial age. The other purpose is to infer the sizes and durations of carbon perturbations in the past by comparing model results with various recorders of environmental change.

Scaling laws represent a powerful synthesis of important dynamics in many systems, illustrating in particular how different combinations of parameters may yield the same result and highlighting particular parameters to which the solution is sensitive. Additionally, they offer a simple way to infer the size and duration of emission events from paleoclimate observations. In the model which we use here, the "long-term" steady-state balance of atmospheric CO$_2$ is assumed to be set by the balance of CO$_2$ rates of input via background volcanic processes and the rates of removal via the weathering of silicates and subsequent burial of marine carbon-
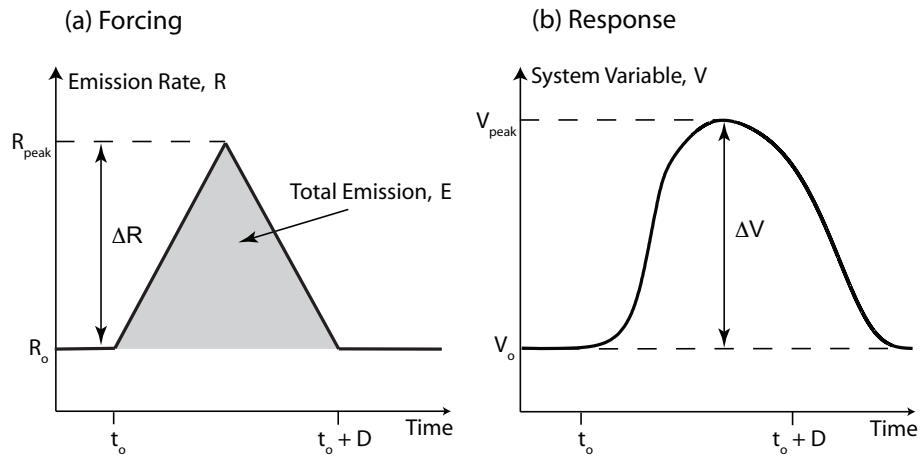
(a) Forcing

(b) Response

Figure 1. Schematic representations of the forcing and nature of system response. **(a)** Triangular atmospheric CO_2 perturbation characterized by duration, D, and total size of emission, E. **(b)** Typical system variable response to forcing. We define the peak system response as $\Delta V = |V_{peak} - V_o|$.

ate sediments (Walker et al., 1981; Berner and Kothavala, 2001; Berner and Caldeira, 1997; Zeebe, 2012b; Uchikawa and Zeebe, 2008). This steady-state balance is thought to be achieved on timescales > 100 kyr. Representing the weathering rate by

$$F_{si} = F_{si}^0 \, (pCO_2)^{nsi}, \tag{1}$$

where F_{si}^0 is the constant background weathering rate and pCO_2 is the atmospheric partial pressure of carbon dioxide, this balance yields $pCO_2 \propto (E/D)^{1/nsi}$, where is E the total emission and D is the duration over which the carbon is emitted. In this limit, the climate is extremely sensitive to the strength of the weathering parameter, nsi.

The purpose of this paper is to examine whether a similar set of scaling laws exists for large emissions with timescales much shorter than millions of years. Given the variety of timescales involved in the interactions between the different carbon reservoirs, it is by no means certain that such scalings exist. We show that they do, but that their actual values depend on the basic state of the system. The scalings thus provide a way to quantify the stability of the carbon cycle through Earth history.

Our scalings characterize the response of the Earth system to emission events with sizes ranging from hundreds to tens of thousands petagrams of carbon (PgC) and durations ranging from 1000 years to 100 000 years. In principle this information could be generated using three-dimensional Earth system models, as it has been for anthropogenic perturbations (Sarmiento et al., 1998; Matsumoto et al., 2004). However, relatively few of the comprehensive Earth system models used to project century-scale climate change include interactions with the sediments (an exception being the Bergen Climate Center of Tjiputra et al., 2010). A number of Earth system models of intermediate complexity (e.g. GENIE-1

Ridgwell et al., 2007) do, however, include these interactions with the sedimentary reservoir. Both the comprehensive and intermediate complexity Earth system models require very long run times (on the order of hundreds of thousands of years) in order to capture the entire history of a perturbation. This represents a significant computational burden, making it difficult to rapidly explore the variety of emission totals and timescales needed to generate scaling laws. Accordingly, in this study we adopt a more streamlined approach, using a simplified Earth system model suitable for representing the carbon cycle on 100 000-year timescales and focusing our attention on perturbations to globally averaged properties rather than local effects.

In this paper we find scaling laws that link perturbations of Earth system variables to atmospheric CO_2 emission size and duration. We use the Long-term Ocean-atmosphere-Sediment CArbon cycle Reservoir (LOSCAR) model (Zeebe et al., 2009; Zeebe, 2012b) to determine quantitative relationships between the magnitude of perturbations to Earth system variables such as atmospheric CO_2, ocean acidity, and alkalinity, and carbon isotope anomalies and idealized transient CO_2 emissions that differ only in terms of their duration and total size. Analyzing the system response to such CO_2 emissions ranging in total size from 50 to 50 000 PgC and durations from 50 years to 100 kyr, we find that most Earth system variable perturbations can be scaled using power law formulas. As these power laws depend on the physical setup, they represent a compact way of characterizing how different climates respond to large transient perturbations.

2   Methods

Figure 1 is a schematic illustrating the type of forcing considered in this study and the nature of the Earth system re-

sponse. Figure 1a shows a CO_2 emission event with a symmetric, triangular-shaped emission rate history superimposed on a steady background emission rate, R_o. This background emission represents the steady-state injection of carbon into the atmosphere from volcanic and metamorphic sources. The transient emission starts at time t_o and ends at time $t_o + D$, so that D is its duration. The total emission in the event, E, is related to its duration and peak emission rate, R_{peak}, by $E = D\Delta R/2$, where $\Delta R = R_{peak} - R_o$. By virtue of the assumption of symmetry, R_{peak} occurs at time $t_o + D/2$. Figure 1b shows the response of a typical system variable, V. The system variable changes with time from its initial value V_o, to its peak value, V_{peak}, and then relaxes back toward V_o. We define the peak system response as $\Delta V = |V_{peak} - V_o|$, the absolute value being necessary in this definition because some system variables respond with negative perturbations. In this study we seek mathematical relationships connecting ΔV to D and E.

LOSCAR is a box model designed for these objectives. It has been employed to investigate a range of problems for both paleo- and modern-climate applications. LOSCAR allows for easy switching between modern and Paleocene and Eocene ocean configurations. It has specifically been used to study the impacts of large transient emissions such as those found during the Paleocene–Eocene Thermal Maximum (PETM), as well as modern anthropogenic emissions. For the modern Earth, LOSCAR components include the atmosphere and a three-layer representation of the Atlantic, Indian, and Pacific (and Tethys for the paleo-version) ocean basins, coupled to a marine-sediment component (Zeebe, 2012b). The marine-sediment component consists of sediment boxes in each of the major ocean basins arranged as functions of depth. The ocean component includes a representation of the mean overturning circulation as well as mixing. Biological cycling is parameterized by restoring surface nutrients to fixed values. In the simulations described here, the circulation and target surface nutrients are kept independent of climate change, so that we focus solely on contrasting surface weathering and sedimentary responses. Biogeochemical cycling in LOSCAR also includes calcium carbonate ($CaCO_3$) dissolution, weathering and burial, silicate weathering and burial, calcite compensation, and carbon fluxes between the sediments, the ocean basins, and the atmosphere. Carbonate dissolution is limited by including variable sediment porosity. In addition, LOSCAR includes a high-latitude surface-ocean box without sediments but otherwise coupled to the other ocean basins through circulation and mixing. Table 3 lists the important model variables, including their notation and dimensional units.

A present-day configuration of LOSCAR has been used to show how a decrease in ocean pH is sensitive to carbon release time, specifically for possible future anthropogenic release scenarios (Zeebe et al., 2008), to determine whether enhanced weathering feedback can mitigate future pCO_2 rise (Uchikawa and Zeebe, 2008), to study effects of increasing ocean alkalinity as a means of mitigating ocean acidification and moderate atmospheric pCO_2 (Paquay and Zeebe, 2013), and to compare modern perturbations with those inferred during the PETM in order to assess the long-term legacy of massive carbon inputs (Zeebe and Zachos, 2013).

For paleoclimate applications LOSCAR has been used to constrain the transient emission needed to produce the observed Earth system responses found during the PETM (Zeebe et al., 2009) and, more generally, to investigate the response of atmospheric CO_2 and ocean chemistry to carbon perturbations throughout the Cenozoic with different forms of seawater chemistry and bathymetry (Stuecker and Zeebe, 2010). Particular applications include constraining the range of the pH effects on carbon and oxygen isotopes in organisms during the PETM perturbation (Uchikawa and Zeebe, 2010), investigating the effects of weathering on the [Ca^{2+}] inventory of the oceans during the PETM (Komar and Zeebe, 2011), inferring changes in ocean carbonate chemistry using the Holocene atmospheric CO_2 record (Zeebe, 2012a), and investigating different processes that potentially generated large-scale fluctuations in the calcite compensation depth (CCD) in the middle to late Eocene (Pälike et al., 2012). Other applications include the analysis of perturbations to the carbon cycle during the Middle Eocene Climatic Optimum (MECO) (Sluijs et al., 2013) and the study of the effects of slow methane release during the early Paleogene (62–48 Ma) (Komar et al., 2013).

3 Case study results

In order to illustrate the dynamics in LOSCAR we examine its response to an idealized emission event of the type shown in Fig. 1 with size $E = 1000$ PgC and duration $D = 5$ kyr. This particular example was initialized in the modern LOSCAR configuration using steady-state preindustrial conditions with an atmospheric $pCO_2 = 280$ ppmv corresponding to a total atmosphere carbon content of $TC_{atm} = 616$ PgC. The initial total carbon content of the global oceans was $TC_{ocn} = 35\,852$ PgC, and the initial global ocean total alkalinity (TA) was $TA = 3.1377 \times 10^{18}$ mol. The emission event began 100 years after startup and its duration is indicated by shading in the figures. This calculation, like all of the others in this study, spans 5 Myr in order to ensure that final steady-state conditions are reached.

The resulting changes in total ocean and atmosphere carbon, TC_{ocn} and TC_{atm} respectively, are shown in Fig. 2a as functions of time in log units. The atmosphere peak perturbation occurs about 3700 years after emission onset, whereas the ocean perturbation peaks about 26 400 years after emission onset. There is an inflection point in the atmosphere response corresponding to the peak ocean response. The leveling out of the atmospheric perturbation is due to ocean–sediment interactions.
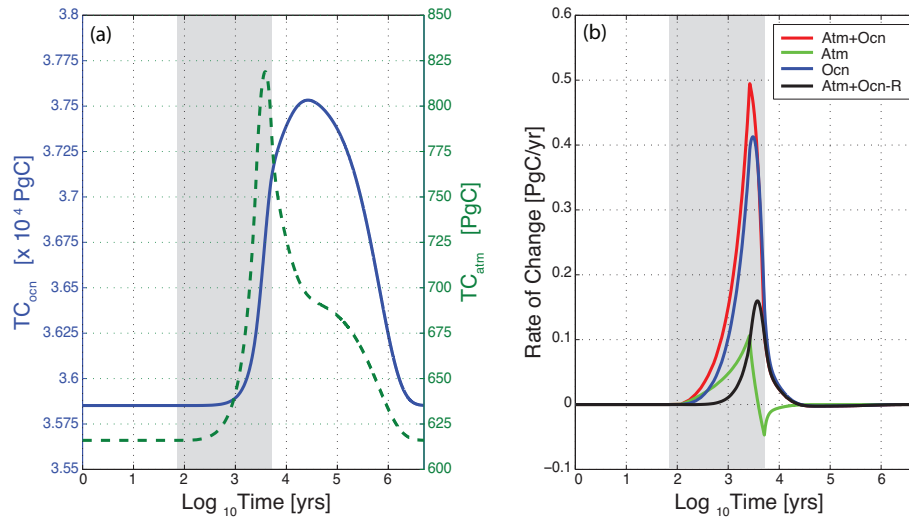
Figure 2. System response as a function of time for the case of $E = 1000\,\text{PgC}$ and $D = 5\,\text{kyr}$. Shaded regions indicate time of emission. **(a)** Total carbon in the atmospheric (green dashed line) and oceanic (blue solid line) reservoirs. **(b)** Corresponding rates of change. System total is shown in red, ocean in blue, atmosphere in green, and the fluxes resulting from feedbacks in the carbon system to the applied emission R in black.
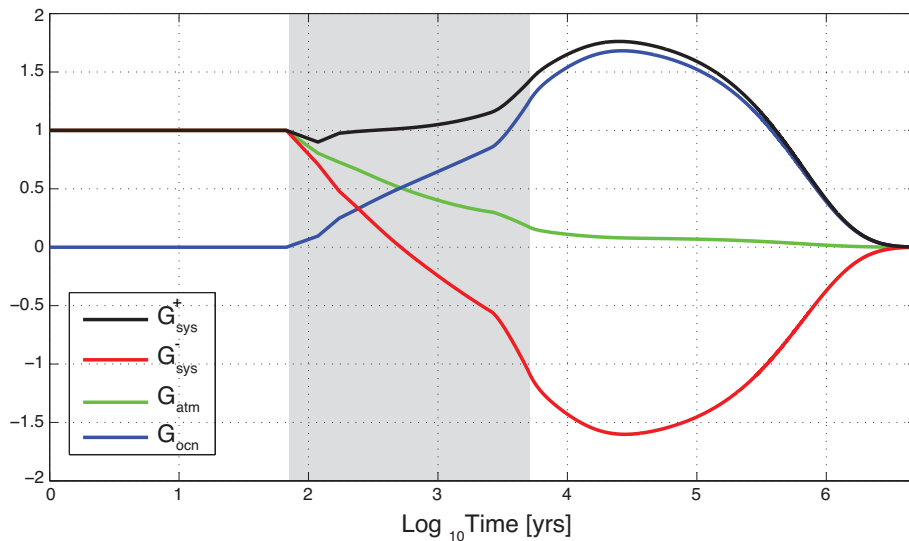

Figure 3. System gain factors as a function of time for the case of $E = 1000\,\text{PgC}$ and $D = 5\,\text{kyr}$. Shaded region indicates time of emission.

Figure 2b shows the corresponding rates of change in TC_{ocn} and TC_{atm}. The curves labeled Atm and Ocn are the time derivatives from Fig. 2a, and the curve labeled Atm+Ocn is their sum. Also shown in Fig. 2b is the adjusted total, the difference between the total rate of change in the atmosphere + ocean and $R - R_o$. The adjusted total, which corresponds to the rate at which additional carbon is added to the ocean–atmosphere system through the reactive processes of weathering, $CaCO_3$ dissolution, and calcite compensation, peaks at $0.16\,\text{PgC yr}^{-1}$ and is positive for about the first 10 kyr after emission onset. This behavior demonstrates how these reactive processes amplify the total carbon

perturbation to the system coming directly from an emission event. The logarithmic timescale (necessary to capture both the fast rise and slow falloff of the carbon perturbation) obscures the important fact that these reactive processes play a quantitatively significant role, accounting for a significant fraction of the large rise in oceanic carbon that occurs after the atmospheric peak.

Because additional carbon enters the system through reactive processes of weathering and marine-sediment dissolution and leaves the system through deposition, the total carbon perturbation at any given time generally does not equal the total emission up to that time. To quantify this effect we

define gain factors, which are ratios of total carbon perturbation to total emission E measured at time t. For the atmosphere and ocean, these are

$$G_{atm}(t) = \frac{TC_{atm}(t) - TC_{atm}(t_o)}{E(t)} \tag{2}$$

and $G_{ocn}(t) = \frac{TC_{ocn}(t) - TC_{ocn}(t_o)}{E(t)}. \tag{3}$

We also define gain factors for the ocean–atmosphere system as

$$G_{sys}^{+}(t) = G_{atm}(t) + G_{ocn}(t) \tag{4}$$

and $G_{sys}^{-}(t) = G_{atm}(t) - G_{ocn}(t). \tag{5}$

According to these definitions, G_{sys}^{+} is the gain of the system as a whole. G_{sys}^{-} gives information on the time-dependent partitioning of carbon between the atmosphere and ocean reservoirs. After emissions onset a value of $0 < G_{sys}^{-} < 1$ indicate that the atmospheric reservoir contains the predominant fraction of the perturbation. The zero crossing of G_{sys}^{-} indicates the time when the relative system response is equivalent in the atmosphere and ocean reservoirs. Values of $G_{sys}^{-} < -1$ indicate that the system has amplified the perturbation, with the majority of the additional carbon being found in the ocean reservoir.

Figure 3 shows these gain factors as a function of time for the emission event from Fig. 2. G_{atm} decreases monotonically over the duration of the emission; the small residual in G_{atm} following the emission shows the long tail of the lifetime of the carbon in the atmosphere (Archer et al., 2009). In contrast, G_{ocn} rises during the emission and continues to increase until it peaks at 1.68, about 26 450 years after emission onset, then decreases to unity after about 380 000 years, and finally returns to 0. Similarly, G_{sys}^{+} generally rises during the emission, peaking at a value of 1.76 around 25 000 years after emission onset, then decreasing to unity after around 408 000 years. G_{sys}^{-} is almost a mirror image of G_{ocn}, indicating that the sediments are contributing more carbon to the ocean than to the atmosphere during this time.

The response of the ocean layers is shown in Fig. 4. Figure 4a shows the time variations in pH in each ocean layer as well as the global ocean total alkalinity. Note that pH variations lead TA in time; first pH drops and TA begins to rise in response, then pH recovers and later TA recovers. The minima in the ocean surface-, intermediate-, and deep-layer pH occur about 3600, 3800, and 4600 years, respectively, after emission onset. In contrast, the maximum TA occurs about 30 500 years after emission onset (by which time the pH is almost fully recovered) and the TA does not fully recover for more than one million years.

The effects of the emission event on Atlantic Ocean sediments are shown in Fig. 4b. The deeper sediments respond earlier and take longer to recover from the perturbation compared to the shallower sediments. In addition, the sediments

at 5000 and 5500 m depths do not recover monotonically but instead overshoot their initial state, becoming relatively enriched in carbonate for tens of thousands of years. This transient enrichment process has been explained in Zachos et al. (2005) as a direct consequence of the weathering feedback, where the enhanced weathering, due to elevated pCO_2, increases the ocean saturation state and deepens the CCD to balance the riverine and burial fluxes.

Figure 4c shows the volume-weighted average temperature perturbations. Peak temperature perturbations occur between 3700 and 4900 years after emission onset, although the atmospheric temperature remains elevated for longer periods due to coupling with pCO_2 in the atmosphere, which has an extended lifetime for up to millions of years, depending on the strength of prescribed weathering feedbacks (Archer et al., 2009; Komar and Zeebe, 2011).

Figure 5 shows the sediment carbonate content for each ocean basin as a function of depth, with colors indicating the starting (red), maximum (light blue), and minimum (dark blue) values that were recorded in each depth box. The deep boxes are most perturbed because they are directly affected by the movement of the CCD. In addition, sediments in the deep Atlantic are perturbed more than those in the Pacific or Indian basins because the CCD is deeper in the Atlantic. Far more carbon enrichment occurs in the Atlantic; for example, the 5000 m box starts at 22 % carbonate and during the run increases to close to 50 %.

Figure 6 shows the time derivative of global TA for the aforementioned case. The red curve accounts for the known contributions of TA from weathering feedbacks and therefore depicts the alkalinity flux that is due to the dissolution and subsequent burial of marine carbonates. Where the red curve is positive, it denotes a net dissolution of carbonates; where it is negative, it denotes a net burial of carbonates. The peak fluxes occur about 3600 years after emission onset, simultaneous with the peak in the average surface pH. Figure 6 shows the dominance of sediment processes in determining the total alkalinity. In this simulation $\approx 80\%$ of the maximum flux of alkalinity to the ocean is due to the dissolution of sediments, which helps to explain the relatively minor role played by weathering in determining the peak atmospheric carbon dioxide.

Figure 7 shows the $\delta^{13}C$ isotope signature for the atmosphere and ocean boxes as a function of time for the case of $E = 1000\,\text{PgC}$ and $D = 5\,\text{kyr}$. The signatures of the surface, intermediate, and deep lines were defined by calculating the volume-weighted average across basins. The atmosphere and surface-ocean perturbations are felt before the deeper ocean boxes. The peak surface signature is around 4000 years after emission onset. The peak deep signature occurs about 5400 years after emission onset, more than 1300 years after it peaks at the surface.
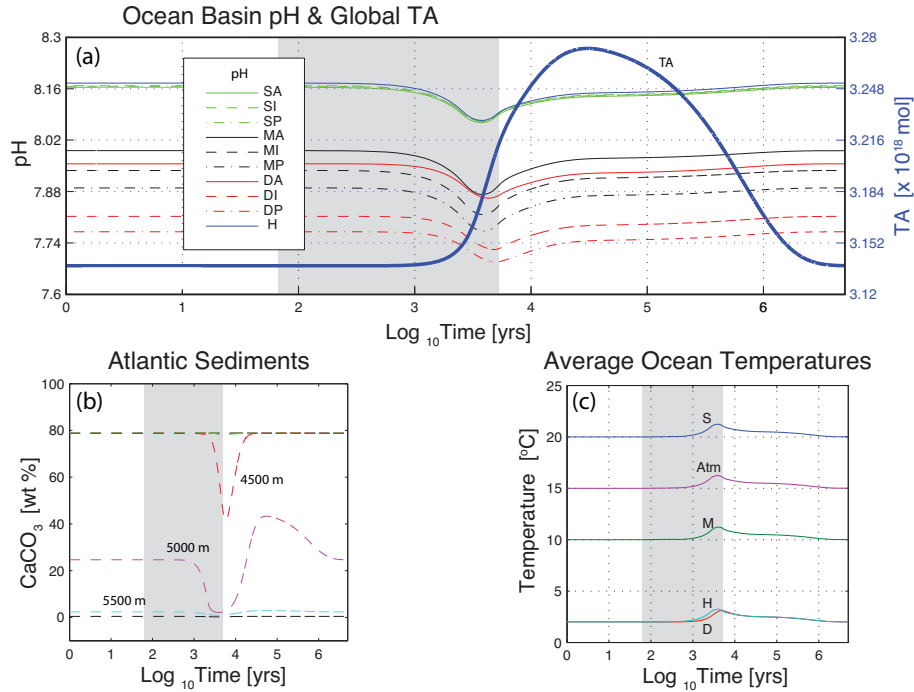
Figure 4. System variables as a function of time for the case of $E = 1000\,\text{PgC}$ and $D = 5\,\text{kyr}$. Shaded regions indicate time of emission. **(a)** Thin lines are pH for the surface (S), intermediate (M), and deep (D) ocean boxes in the Atlantic (A), Indian (I), and Pacific (P) basins. Thick solid line is the global ocean total alkalinity (TA). **(b)** $CaCO_3$ wt % of sediment boxes within the Atlantic Basin. **(c)** Temperature for atmosphere (Atm) and high-latitude boxes (H). Surface (S), intermediate (M), and deep (D) ocean temperatures are averages across basins..

Figure 5. Extreme $CaCO_3$ contents in each ocean basin as a function of sediment depth for the case of $E = 1000\,\text{PgC}$ and $D = 5\,\text{kyr}$.

Figure 6. Time rate of change in global total alkalinity (TA) for the case of $E = 1000\,\mathrm{PgC}$ and $D = 5\,\mathrm{kyr}$. Shaded region indicates time of emission. Blue curve is the time rate of change in global ocean TA. Red curve shows the blue curve minus the TA flux that is due to weathering feedbacks.

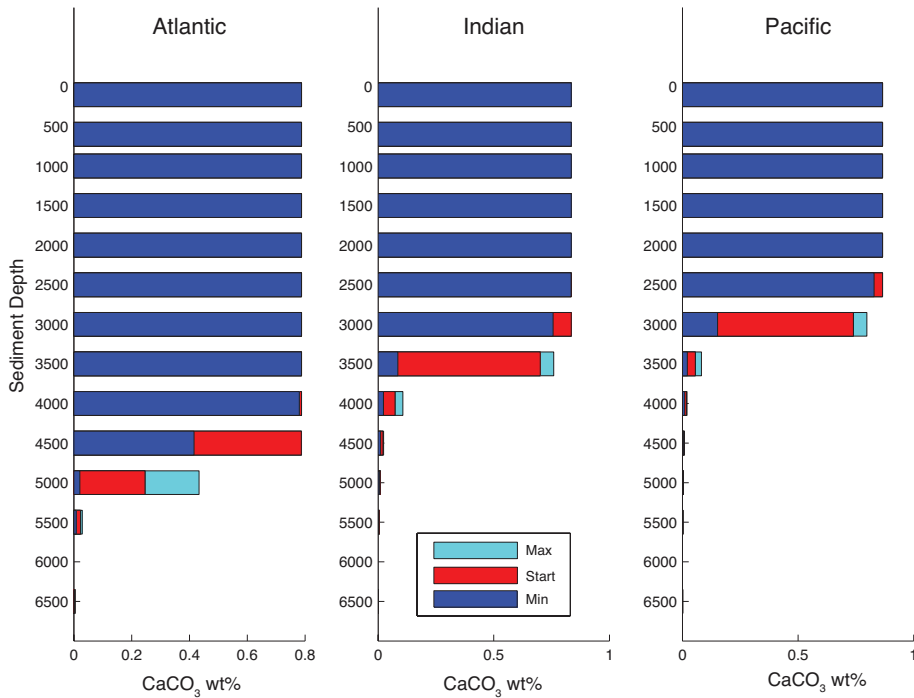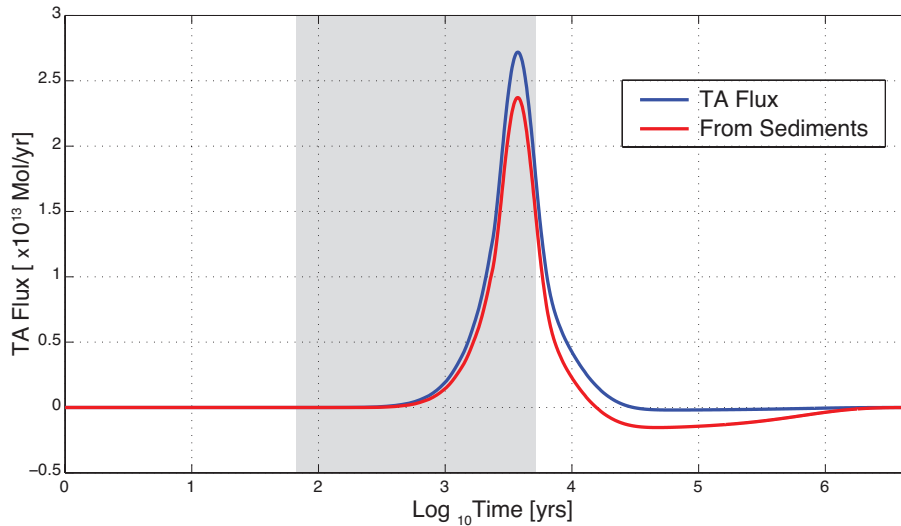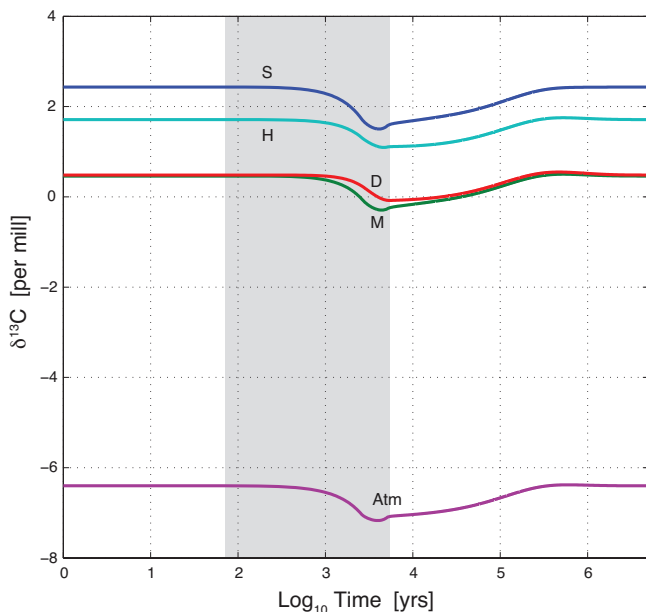**Figure 7.** Carbon-13 isotope signature for the atmosphere (Atm) and ocean boxes as a function of time for the case of $E = 1000\,\mathrm{PgC}$ and $D = 5\,\mathrm{kyr}$. The surface (S), intermediate (M), and deep (D) boxes were averaged for all basins. H is high-latitude box. Shaded region indicates time of emission.

4   Power law scalings

Table 1 compares two cases which differ in D and E but share the same ΔR. If the system response was linear, the perturbations in these two cases would be in proportion to E, i.e., they differ twenty-fold in their response. However,

Table 1. Comparison of cases.

ΔV	Units	Case 1 $D = 1\,\mathrm{kyr}$ $E = 1000\,\mathrm{PgC}$	Case 2 $D = 100\,\mathrm{kyr}$ $E = 20\,000\,\mathrm{PgC}$	Case 2 : Case 1
$\mathrm{TC_{atm}}$	PgC	158.313	2123.627	13.41
$\mathrm{TC_{ocn}}$	PgC	0.1681×10^4	3.0729×10^4	18.28
TA	mol	0.1354×10^{18}	2.4707×10^{18}	18.25
$\delta^{13}\mathrm{C_{atm}}$	‰	1.009	3.550	3.52
$\delta^{13}\mathrm{C_S}$	‰	1.036	4.775	4.61
$\delta^{13}\mathrm{C_M}$	‰	0.686	4.955	7.22
$\delta^{13}\mathrm{C_D}$	‰	0.873	12.188	13.96

Table 1 shows that none of these variables are in the proportion of 20 : 1. For a nonlinear response that depends only on ΔR, these variables would be in constant proportion other than 20 : 1. This is not the case either. Accordingly, a more general formulation is needed to systematize these results.

A power law relationship between the peak change in a system variable ΔV and the total magnitude and duration of the emission event shown in Fig. 1 can be written as

$$\Delta V = \gamma D^\alpha E^\beta, \tag{6}$$

where the coefficient γ and the exponents α and β assume different values for each system variable. Alternatively, Eq. (6) can be written in terms of emission rate using $\Delta R = 2E/D$:

$$\Delta V = 2^{-\beta} \gamma D^{\alpha+\beta} \Delta R^\beta = 2^\alpha \gamma E^{\alpha+\beta} \Delta R^{-\alpha}. \tag{7}$$

If the peak change in ΔV depends only on the peak emissions rate, ΔR, then $\alpha = -\beta$ in Eqs. (6) and (7). Other simple balances are possible. For example, it may be that the

Table 2. Summary of weathering strength variations considered.

nsi	0.20*	0.20	0.20	0.20	0.20	0.025	0.10	0.40	2.0
ncc	0.40*	0.025	0.05	0.80	2.0	0.40	0.40	0.40	0.40

* indicates LOSCAR default values.

Table 3. Variable definitions and symbols used.

Variable	Symbol	Units
Atmosphere	atm	NA
Ocean	ocn	NA
Sediments	sed	NA
High-latitude, Atlantic, Indian, Pacific basins	H, A, I, P	NA
Surface-, intermediate-, deep-ocean boxes	S, M, D	NA
Emissions rate	R	PgC yr^{-1}
Emissions duration	D	yr
Total emissions	E	PgC
System variable	V	Varies
Coefficient	γ	Varies
Duration scaling exponent	α	ND
Emissions scaling exponent	β	ND
Global total alkalinity	TA	mol
pH	pH	ND
Temperature	T	°C
Sediment carbonate weight %	% CaCO$_3$	ND
Time	t	yr
Total atmospheric carbon	TC$_{\text{atm}}$	PgC
Total oceanic carbon	TC$_{\text{ocn}}$	PgC
Carbon-13 isotope	$\delta^{13}\text{C}$	‰
Volcanic degassing flux	F_{vc}	PgC yr^{-1}
Air–Sea gas exchange flux	F_{gas}	PgC yr^{-1}
Carbonate weathering flux	F_{cc}	PgC yr^{-1}
Silicate weathering flux	F_{si}	PgC yr^{-1}
Emissions flux	R'	PgC yr^{-1}
Silicate weathering exponent	nsi	ND
Carbonate weathering exponent	ncc	ND
Calcite compensation depth	CCD	km
Carbonate ion	CO_3^{2-}	mol

peak values depend on the actual time-varying emissions rate $R'(t) = R(t) - R_o$. Our scaling analysis considers only the peak values of the perturbed variables. To determine global ocean carbon content, we multiplied the dissolved inorganic carbon (DIC) concentrations in each of the ocean boxes by their prescribed volumes to obtain the total mass of carbon in each box. We then summed over all the ocean boxes to define the variable TC$_{\text{ocn}}$. We used this same procedure to determine the global ocean total alkalinity. For the analysis of temperature, $\delta^{13}\text{C}$, and pH, we calculated the volume-weighted averages for the surface-, intermediate-, and deep-ocean boxes, respectively. Once peak variables were obtained, we performed a regression analysis against D and E for each system variable.

The results of this procedure for TC$_{\text{atm}}$, TC$_{\text{ocn}}$, and TA are shown in Figs. 8–10. Figures 8a, 9a, and 10a show the unscaled peak changes in these variables vs. E for different D values. ΔTC$_{\text{atm}}$ has a distinct dependence on D, whereas

ΔTC$_{\text{ocn}}$ and ΔTA have virtually none. Figures 8b, 9b, and 10b show the peak changes scaled according to Eq. (6). The peak changes in Figs. 9b and 10b vary linearly with emissions size E, and accordingly the scaled results collapse to a power law fit with negligible deviation. In Fig. 8b, however, the power law behavior of the ΔTC$_{\text{atm}}$ fit is limited to the range $10^2 < E < 10^4$ PgC. The deviation at the upper end of this range is due to the fact that the carbonate sediments cannot be dissolved without limit; at some point the accessible carbon reservoir in the sediments becomes exhausted.

Tables 4–6 give the results of our power law scalings for the modern LOSCAR configuration in terms of best-fitting values for the exponents α and β, the preexponential coefficient γ, and the R value of the fit. Although $\alpha < 0$ and $\beta > 0$ for all variables, as expected, large differences in some of the exponents are evident. For example, TC$_{\text{atm}}$ and TC$_{\text{ocn}}$ have very different dependences on duration D, with the atmosphere exponent having a value of $\alpha = -0.289$ and the ocean exponent having a value of $\alpha = -0.0035$. These variables also have different β dependences, with the atmosphere exponent having a value of $\beta = 1.174$ and the ocean having a relatively weaker exponent value of $\beta = 0.982$. Note, however, that $\alpha + \beta \simeq 1$ for both of these, as well as for TA. Ocean and atmosphere temperatures generally have smaller β values and $\alpha + \beta$ in the range 0.6–0.8.

Scalings for the $\delta^{13}\text{C}$ variables in the atmosphere and in the upper and intermediate-ocean boxes show dependence on duration, while the deep-ocean box shows negligible dependence. This result suggests that by using the isotopic signatures from organisms from different depths that were deposited at the same time, one could explicitly solve for the E and D that produced that particular isotopic excursion. In general, the duration dependence of ocean variables weakens going downward from the surface.

5 Power law scalings for the Paleocene and Eocene

Following the same procedures as in the previous section, we conducted a scaling analysis for the Paleocene and Eocene version of LOSCAR, which has different boundary and initial conditions than the modern version. Notable differences include the addition of the Tethys Ocean basin, higher ocean temperatures, and different seawater chemistry, steady-state weathering fluxes, and ocean circulation patterns. The detailed descriptions of this model configuration can be found in Zeebe (2012b).

Table 4. Power law scalings for modern configuration, global variables, and $\Delta V = \gamma D^\alpha E^\beta$. D in yr and E in PgC.

V	Units	γ	α	β	R value
TC_{atm}	PgC	0.805	-0.289	1.174	0.988
T_{atm}	°C	2.580×10^{-2}	-0.200	0.794	0.964
TC_{ocn}	PgC	1.930	-3.556×10^{-3}	0.982	0.999
TA	mol	1.561×10^{14}	-3.467×10^{-3}	0.981	0.999
Max TCO_3^{2-}	mol	2.021×10^{12}	-1.775×10^{-4}	0.965	0.998
Min TCO_3^{2-}	mol	3.201×10^{14}	-0.209	0.736	0.899

Table 5. Power law scalings for modern configuration, $\delta^{13}C$ variables, $\Delta V = \gamma D^\alpha E^\beta$. D in [yr] and E in [PgC].

V	Units	γ	α	β	R value
Min $\delta^{13}C_{atm}$	‰	3.852×10^{-2}	-0.242	0.760	0.954
Min $\delta^{13}C_S$	‰	2.907×10^{-2}	-0.216	0.783	0.966
Min $\delta^{13}C_M$	‰	7.766×10^{-3}	-0.132	0.819	0.979
Min $\delta^{13}C_D$	‰	1.566×10^{-3}	-0.040	0.877	0.989

These simulations were initialized using steady-state pre-PETM conditions with an atmospheric $p\text{CO}_2 = 1000$ ppmv, corresponding to a total atmosphere carbon content of $TC_{atm} = 2200$ PgC. The initial total carbon content of the global oceans was $TC_{ocn} = 34\,196$ PgC, and the initial global ocean total alkalinity (TA) was $TA = 2.7895 \times 10^{18}$ mol. The idealized emission events began 100 years after startup. The run lengths, like in the modern configuration, also spanned 5 Myr in order to ensure that final steady-state conditions were reached. Tables 7–9 give the results of our power law scalings for this configuration.

A comparison of the scalings shows that the responses to transient perturbations are qualitatively similar across the two climates. Figures 13–15 show the correlations of peak perturbations in the two configurations. For most emission events the correlation is high; however, there are systematic deviations for some variables. For example, the paleo-ocean systematically takes up less carbon than the modern ocean (Fig. 13b), leaving more in the atmosphere (Fig. 13a). This is likely to be due to higher paleo-temperatures and lower alkalinities resulting in weaker ocean buffering capacity. The changes in pH, however, are systematically larger in the modern ocean compared to the paleo-ocean(Fig. 14a). The relatively small changes in carbonate chemistry are unlikely to explain the systematics (doubling $p\text{CO}_2$ with the paleo-surface-temperature of 25 °C and an alkalinity of 2000 µM gives almost the same change in pH as a modern temperature of 20°C and an alkalinity of 2300 µM). The differences in pH are possibly due to differences in the carbonate weathering feedbacks or because the ocean circulation is stronger in the paleo-version. Carbon-13 anomalies tend to be smaller at the surface in the paleo-version, but the deep anomalies are essentially identical in both (Fig. 15).

6 Scaling law exponent sensitivity to variations in weathering feedbacks

Examples of system variable sensitivity to nsi and ncc, within LOSCAR, have been explored in previous studies (Uchikawa and Zeebe, 2008; Komar and Zeebe, 2011), but the relative range of the values studied was restricted by only considering enhanced feedbacks due to nominal values of these parameters (Zeebe, 2012b). Here we consider a broader range of these values in the modern LOSCAR configuration to determine α and β sensitivity to large variations in the strength of these feedbacks. Table 2 shows the cases considered.

Figure 11 shows the resulting α and β values for the cases in Table 2 for the peak changes in TC_{atm}, TC_{ocn}, and TA. Figure 11a shows that, as ncc increases while nsi is held at the default value, the resulting α values for TC_{atm} become more negative. Increasing nsi while holding ncc at the default value also results in more negative α values. Figure 11b shows that, as ncc increases while nsi is held at the default value, the resulting β values for TC_{atm} monotonically decrease. Increasing nsi while holding ncc at the default value also results in smaller β values. Figure 11c shows that. as ncc increases while nsi is held at the default value, the resulting α values for TC_{ocn} decrease negligibly. Increasing nsi while holding ncc at the default value also results negligible changes in α values. Figure 11d shows that, as ncc increases while nsi is held at the default value, the resulting β values for TC_{ocn} monotonically increase. Increasing nsi while holding ncc at the default value produces monotonically decreasing β values. Figure 11e shows that increasing ncc while holding nsi at the default value yields negligible changes in α values for TA. Increasing nsi while holding ncc at the default value also results in negligible changes in the α values. Figure 11f shows that, as ncc increases while nsi is

Table 6. Power law scaling for modern configuration, ocean boxes, and $\Delta V = \gamma D^\alpha E^\beta$. D in yr and E in PgC.

V	Units	γ	α	β	R value
TA_S	PgC	4.621×10^{-2}	-3.508×10^{-3}	0.982	0.999
TA_M	PgC	4.122×10^{-1}	-3.513×10^{-3}	0.982	0.999
TA_D	PgC	1.385	-3.467×10^{-3}	0.983	0.999
TA_{HL}	PgC	1.271×10^{-2}	-3.423×10^{-3}	0.982	0.999
$TDIC_S$	PgC	6.436×10^{-2}	-1.776×10^{-2}	0.959	0.998
$TDIC_M$	PgC	0.420	-3.60×10^{-3}	0.982	0.999
$TDIC_D$	PgC	1.454	-3.541×10^{-3}	0.982	0.999
$TDIC_{HL}$	PgC	1.350×10^{-2}	-4.23×10^{-3}	0.979	0.999
T_S	°C	2.473×10^{-2}	-0.196	0.795	0.964
T_M	°C	1.318×10^{-2}	-0.157	0.824	0.968
T_D	°C	4.888×10^{-3}	-0.098	0.863	0.979
Min pH_S	ND	2.365×10^{-3}	-0.249	0.818	0.962
Min pH_M	ND	2.050×10^{-3}	-0.211	0.799	0.940
Min pH_D	ND	5.320×10^{-4}	-0.134	0.853	0.968
Min $CO_3^{2-}{}_S$	mol	5.083×10^{13}	-0.336	0.744	0.887
Min $CO_3^{2-}{}_M$	mol	2.356×10^{14}	-0.256	0.684	0.864
Min $CO_3^{2-}{}_D$	mol	1.522×10^{14}	-0.191	0.751	0.912
Min $CO_3^{2-}{}_{HL}$	mol	8.867×10^{12}	-0.289	0.711	0.894
Max $CO_3^{2-}{}_S$	mol	2.473×10^{11}	-3.223×10^{-3}	0.902	0.994
Max $CO_3^{2-}{}_M$	mol	9.146×10^{11}	-1.595×10^{-4}	0.946	0.998
Max $CO_3^{2-}{}_D$	mol	9.574×10^{11}	8.321×10^{-4}	0.980	0.998
Max $CO_3^{2-}{}_{HL}$	mol	2.013×10^{10}	-9.039×10^{-4}	0.910	0.992
Max CCD_A	km	2.749×10^{-4}	-1.103×10^{-2}	0.837	0.934
Max CCD_I	km	1.279×10^{-5}	-1.298×10^{-2}	1.210	0.955
Max CCD_P	km	4.798×10^{-6}	-9.784×10^{-3}	1.297	0.961
Min CCD_A	km	1.131×10^{-2}	-0.178	0.734	0.904
Min CCD_I	km	6.233×10^{-4}	-0.220	1.046	0.896
Min CCD_P	km	1.908×10^{-4}	-0.189	1.135	0.896

Table 7. Power law scalings for Paleocene–Eocene configuration, global variables, and $\Delta V = \gamma D^\alpha E^\beta$. D in yr and E in PgC.

V	Units	γ	α	β	R value
TC_{atm}	PgC	1.285	-0.151	1.0539	0.994
T_{atm}	°C	9.580×10^{-3}	-0.110	0.778	0.969
TC_{ocn}	PgC	1.482	-1.807×10^{-3}	0.981	0.999
TA	mol	1.130×10^{14}	-1.802×10^{-3}	0.985	0.999
Max TCO_3^{2-}	mol	6.113×10^{11}	-1.954×10^{-3}	1.035	0.983
Min TCO_3^{2-}	mol	4.922×10^{13}	-0.169	0.712	0.909

held at the default value, the resulting β values for TA monotonically increase, similar to the behavior in Fig. 11d. Moreover, increasing nsi while holding ncc at the default value yields smaller β values, like those in Fig. 11d. In summary, Fig. 11 shows that β values are relatively more sensitive to changes in weathering strengths.

7 Discussion

The results presented in the previous section raise a number of important questions. In this section we further examine these, focussing on the following in particular:

Table 8. Power law scalings for Paleocene and Eocene configuration, $\delta^{13}C$ variables, and $\Delta V = \gamma D^\alpha E^\beta$. D in yr and E in PgC.

V	Units	γ	α	β	R value
Min $\delta^{13}C_{atm}$	‰	2.005×10^{-2}	-0.199	0.777	0.963
Min $\delta^{13}C_S$	‰	1.776×10^{-2}	-0.178	0.783	0.969
Min $\delta^{13}C_M$	‰	5.243×10^{-3}	-0.099	0.819	0.981
Min $\delta^{13}C_D$	‰	1.447×10^{-3}	-0.031	0.876	0.990

Table 9. Power law scaling for Paleocene and Eocene configuration, ocean boxes, and $\Delta V = \gamma D^\alpha E^\beta$. D in yr and E in PgC.

V	Units	γ	α	β	R value
TA_S	PgC	0.035	-1.821×10^{-3}	0.983	0.999
TA_M	PgC	0.304	-1.837×10^{-3}	0.984	0.999
TA_D	PgC	1.013	-1.810×10^{-3}	0.985	0.999
TA_{HL}	PgC	8.414×10^{-3}	-1.730×10^{-3}	0.983	0.999
$TDIC_S$	PgC	0.037	-1.811×10^{-3}	0.980	0.999
$TDIC_M$	PgC	0.328	-1.834×10^{-3}	0.981	0.999
$TDIC_D$	PgC	1.103	-1.855×10^{-3}	0.982	0.999
$TDIC_{HL}$	PgC	9.032×10^{-3}	-1.823×10^{-3}	0.982	0.999
T_S	°C	9.180×10^{-3}	-0.108	0.780	0.969
T_M	°C	6.767×10^{-3}	-8.741×10^{-2}	0.792	0.970
T_D	°C	4.251×10^{-3}	-6.027×10^{-2}	0.812	0.976
Min pH_S	ND	1.063×10^{-3}	-0.151	0.782	0.965
Min pH_M	ND	8.839×10^{-4}	-0.136	0.746	0.949
Min pH_D	ND	3.203×10^{-4}	-0.095	0.812	0.970
Min $CO_3^{2-}{}_S$	mol	9.639×10^{12}	-0.190	0.673	0.906
Min $CO_3^{2-}{}_M$	mol	2.637×10^{13}	-0.205	0.649	0.881
Min $CO_3^{2-}{}_D$	mol	2.537×10^{13}	-0.165	0.736	0.916
Min $CO_3^{2-}{}_{HL}$	mol	1.497×10^{12}	-0.184	0.672	0.908
Max $CO_3^{2-}{}_S$	mol	1.378×10^{10}	-2.215×10^{-3}	1.051	0.948
Max $CO_3^{2-}{}_M$	mol	1.914×10^{11}	-1.979×10^{-3}	1.030	0.987
Max $CO_3^{2-}{}_D$	mol	4.115×10^{11}	-2.081×10^{-3}	1.034	0.982
Max $CO_3^{2-}{}_{HL}$	mol	1.373×10^9	-2.000×10^{-3}	1.070	0.927
Max CCD_A	km	4.563×10^{-4}	-1.441×10^{-3}	0.825	0.978
Max CCD_I	km	8.724×10^{-5}	-1.214×10^{-3}	1.007	0.974
Max CCD_P	km	1.772×10^{-5}	-1.833×10^{-3}	1.192	0.955
Max CCD_T	km	4.472×10^{-5}	-1.784×10^{-3}	1.133	0.946
Min CCD_A	km	8.918×10^{-3}	-0.124	0.666	0.911
Min CCD_I	km	2.968×10^{-3}	-0.166	0.805	0.888
Min CCD_P	km	1.409×10^{-4}	-0.173	1.109	0.904
Min CCD_T	km	4.877×10^{-4}	-0.202	0.986	0.840

1. Why is the dependence on weathering so weak?

2. What controls the maximum in CO_2?

3. What does this imply about additional feedbacks in the system?

Considerable insight can be gained into how the maximum pCO_2 is set by noting that the bicarbonate ion concentration at equilibrium is given by

$$[HCO_3^-] = \frac{k_H\ k_1\ pCO_2}{[H^+]}, \tag{8}$$

where k_H is the Henry's law coefficient, k_1 and k_2 are dissociation coefficients, and $[H^+]$ is the hydrogen ion concentration. Similarly, the equilibrium carbonate ion concentration is given by

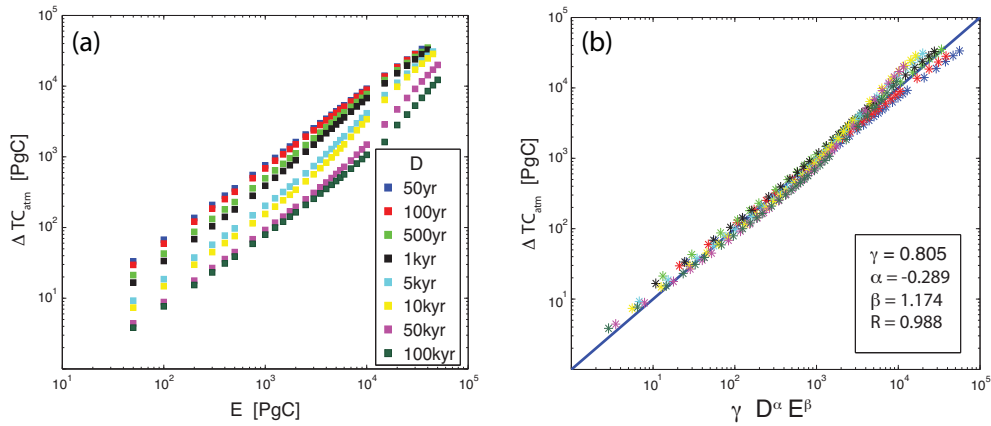$$[CO_3^{2-}] = \frac{k_H\ k_1\ k_2\ pCO_2}{[H^+]^2}. \tag{9}$$

Figure 8. (a) Peak changes in the modern atmospheric total carbon content as a function of total emission, E, for various durations, D. **(b)** Multivariable regression results. Solid line indicates a perfect fit to the predicted scaling. The asterisks are each individual cases.
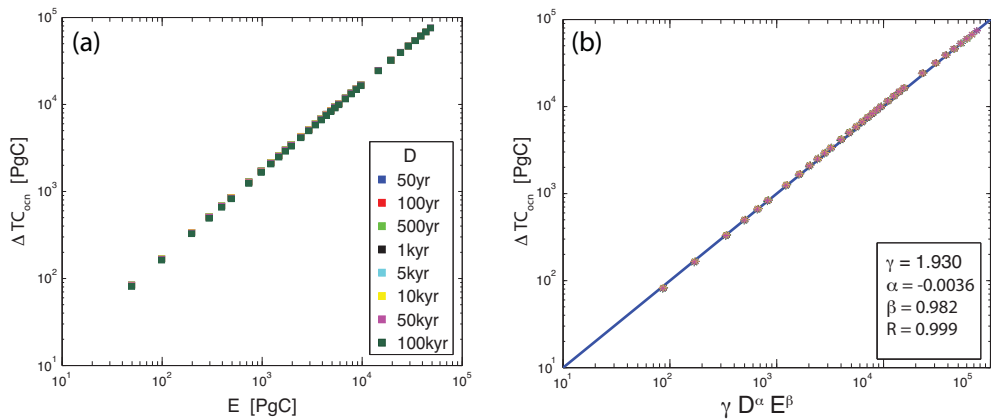

Figure 9. (a) Peak changes in the modern oceanic total carbon content as a function of total emission, E, for various durations, D. **(b)** Multivariable regression results. Solid line indicates a perfect fit to the predicted scaling. The asterisks are each individual cases.

Then we can solve for the $p\mathrm{CO_2}$ from Eqs. (8) and (9)

$$p\mathrm{CO_2} = \frac{k_2}{k_\mathrm{H} k_1} \frac{[\mathrm{HCO_3^-}]^2}{[\mathrm{CO_3^{2-}}]}. \tag{10}$$

Letting DIC be the dissolved inorganic carbon, ALK the carbonate alkalinity, and $\mathrm{C} = k_\mathrm{H} p\mathrm{CO_2}$ the aqueous $p\mathrm{CO_2}$, we find that

$$p\mathrm{CO_2} \approx \frac{k_\mathrm{H}\, k_1}{k_2} \frac{(2\mathrm{DIC} - \mathrm{ALK} + \mathrm{C})^2}{(\mathrm{ALK} - \mathrm{DIC})} \tag{11}$$

When $p\mathrm{CO_2}$ is at a maximum $\partial \mathrm{C}/\partial t$ is likewise 0 so that we can find a relationship between $\partial \mathrm{DIC}/\partial t$ and $\partial \mathrm{ALK}/\partial t$. Taking the derivative with respect to time at the maximum $p\mathrm{CO_2}$,

$$\frac{2(2\,\mathrm{DIC} - \mathrm{ALK} + \mathrm{C})}{(\mathrm{ALK} - \mathrm{DIC})}\left(2\frac{\partial \mathrm{DIC}}{\partial t} - \frac{\partial \mathrm{ALK}}{\partial t}\right)$$
$$-\frac{(2\mathrm{DIC} - \mathrm{ALK} + \mathrm{C})^2}{(\mathrm{ALK} - \mathrm{DIC})^2}\left(\frac{\partial \mathrm{ALK}}{\partial t} - \frac{\partial \mathrm{DIC}}{\partial t}\right) = 0. \tag{12}$$

This can be solved to give us

$$\frac{\partial \mathrm{ALK}}{\partial t} = \frac{3\mathrm{ALK} - 2\mathrm{DIC} + 2\mathrm{C}}{\mathrm{ALK}}\frac{\partial \mathrm{DIC}}{\partial t}. \tag{13}$$

This can also be rewritten as

$$\frac{\partial \mathrm{ALK}}{\partial t} = \frac{[\mathrm{HCO_3^-}] + 4[\mathrm{CO_3^{2-}}]}{[\mathrm{HCO_3^-}] + 2[\mathrm{CO_3^{2-}}]}\frac{\partial \mathrm{DIC}}{\partial t} \tag{14}$$

so that the maximum in $p\mathrm{CO_2}$ is reached when the alkalinity change is a little higher than the DIC change. Since

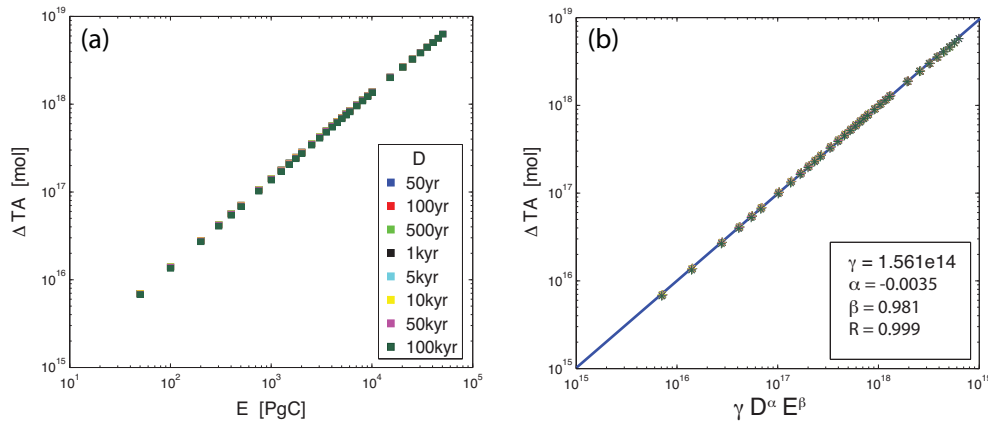$$[\mathrm{HCO_3^-}]/[\mathrm{CO_3^{2-}}] = k_2/[\mathrm{H^+}], \tag{15}$$

Figure 10. (a) Peak changes in the modern global ocean total alkalinity (TA) as a function of total emission, E, for various durations, D. **(b)** Multivariable regression results. Solid line indicates a perfect fit to the predicted scaling. The asterisks are each individual cases.

we can rewrite this as

$$\frac{\partial \mathrm{ALK}/\partial t}{\partial \mathrm{DIC}/\partial t} = \theta = \frac{1 + 4\, k_2/[\mathrm{H}^+]}{1 + 2 k_2/[\mathrm{H}+]}. \tag{16}$$

There are two possible ways for $\partial p\mathrm{CO}_2/\partial t$ to equal 0 in Eq. (11). The first is the equilibrium regime where the emissions occur over very long timescales and the surface changes in TDIC and ALK mirror the ocean-average changes. This is the regime in which we would expect to find a strong dependence on weathering parameters. However, as can be seen from looking at Fig. 12, our transient simulations are characterized by a *dynamic* balance, where both TDIC and TA are changing. This dynamic balance means that it is the growth of alkalinity within the ocean that brings atmospheric $p\mathrm{CO}_2$ into balance. Examining θ at the time of maximum $p\mathrm{CO}_2$ (Fig. 12a) shows that the two terms are approximately the same for all the runs with durations of 10 000, 50 000 and 100 000 years. For surface temperatures of around 20 °C, $k_2 \approx 10^{-9}$ so that the ratio between alkalinity and DIC change is around about 1.2 at low emissions. As the pH increases for longer timescales, this ratio drops towards 1.

For short durations, by contrast, the peak is found when θ is very small. Rather than carbonate reactions being important, what matters is the ability of the ocean circulation to move carbon away from the surface. A careful examination of these cases shows that the bulk of added carbon dioxide resides in the atmosphere.

The relatively weak dependence of θ on total emissions obscures an interesting difference between short- and long-duration pulses. For short-duration pulses, θ increases as the emissions increase. As more and more carbon is added to the system over short periods of time, more of it reacts with calcium carbonate and increases ocean alkalinity. However, for the long-duration simulations, the dependence runs in the opposite direction, with higher emissions showing less compensation from alkalinity.

To first order, a situation in which the growth rates in TDIC and TA are equal is what one would expect in a system without burial, where the additional carbon added to the atmosphere reacts with silicate rocks and the additional alkalinity ends up accumulating in the ocean. Such a situation would also be expected to have a strong dependence on weathering parameters. However, in LOSCAR the dominant flux of alkalinity is often from the sediments to the ocean. This flux will grow not just because the deep-ocean pH decreases but because more sediments are mobilized as this happens.

At intermediate durations the picture becomes much more complicated. There appears to be an optimal emission for maximizing interactions with the sediments. The reasons for this are unclear, but it is striking that the timescales involved are similar to the timescales for ocean overturning.

Note that the discretization of the deep ocean into a fixed number of boxes introduces some step-like behavior into the volume of sediments mobilized, which can be seen in Fig. 12b. The fact that less sediment is available for interaction as the lysocline shallows may explain part of why θ drops at high emission in Fig. 12b. In any case, we expect the sediment alkalinity flux to have a functional dependence on the perturbation DIC, which is linear or superlinear, implying that it has the potential to overwhelm the rather weak dependence on $p\mathrm{CO}_2$.

Our results suggest future sensitivity studies. For example, what differences between the Paleocene and Eocene and modern world produce different scaling laws? Answers might be found in different ocean circulation patterns or different hypsometric distributions, which would then determine the amount of sediment available to react with CO_2.

Additionally, the strong role played by the oceanic carbonate budget suggests additional feedbacks involving the biological pump. In the version of LOSCAR used here, the removal of organic material from the surface layer is primarily controlled by high-latitude nutrients and the ocean circulation, neither of which varies with CO_2 in our simulations.
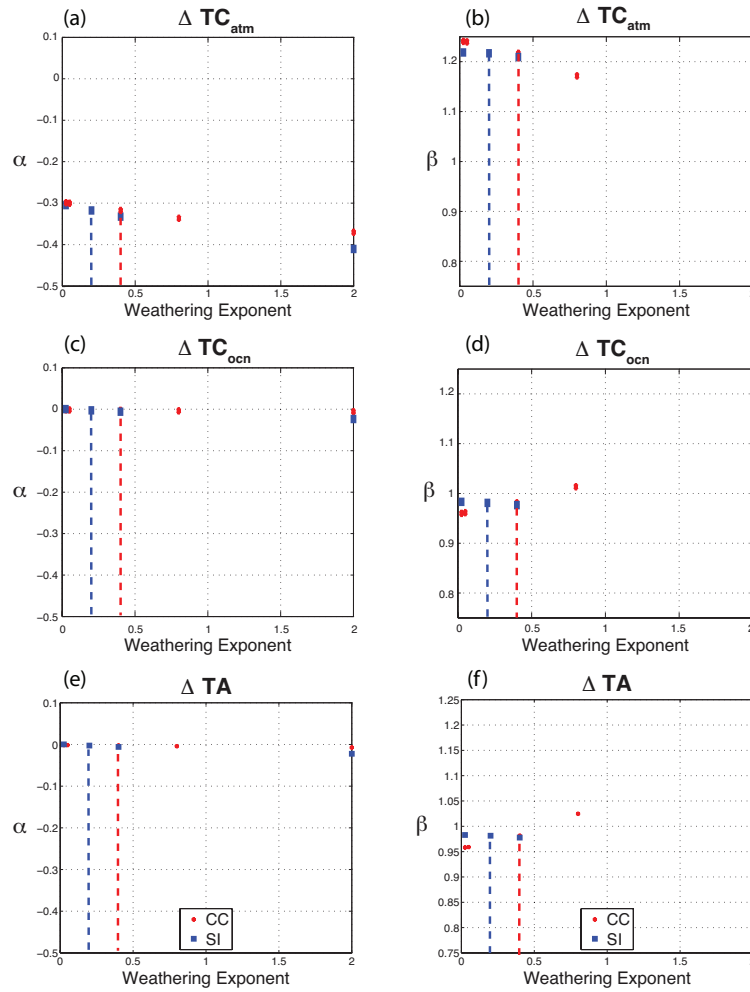
Figure 11. Sensitivity of scaling results to variations in weathering exponents. Dashed lines indicate default LOSCAR exponent values (ncc = 0.40; nsi = 0.20). **(a, b)** Peak total atmospheric carbon; **(c, d)** peak total ocean carbon; **(e, f)** peak global total alkalinity (TA).
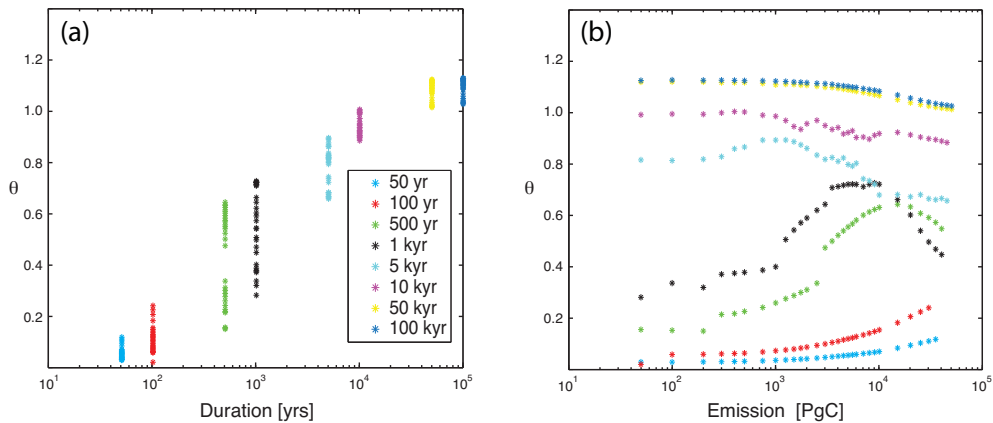

Figure 12. Ratio of the rate of change in total global dissolved inorganic carbon to the rate of change in global total alkalinity **(a)** vs. duration, at the time of maximum pCO$_2$, and **(b)** vs. emission, at the time of maximum pCO$_2$.
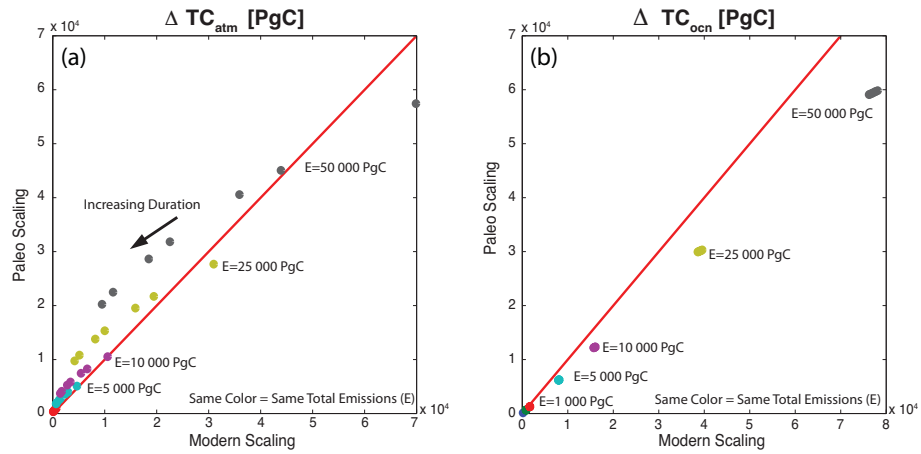
Figure 13. Correlation between peak perturbations for modern and paleo-scalings. **(a)** Total atmospheric carbon. **(b)** Total oceanic carbon. Same color denotes same total emissions.
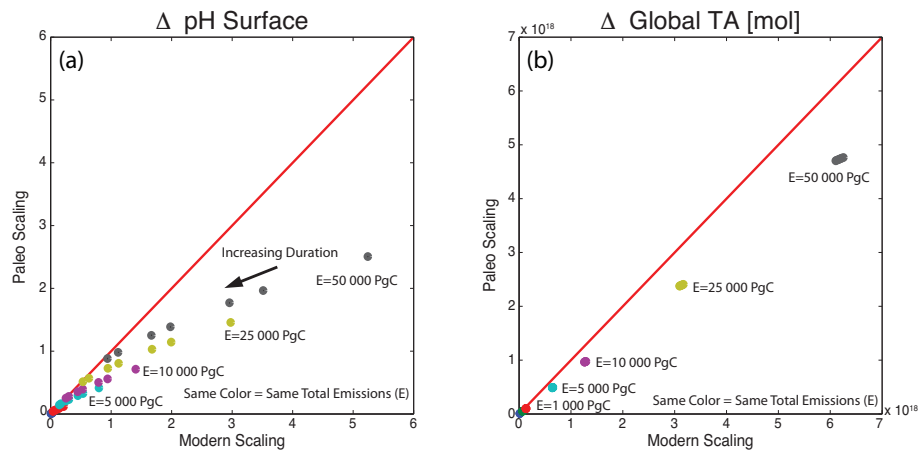
Figure 14. Correlation between peak perturbations for modern and paleo-scalings. **(a)** Surface pH. **(b)** Total global alkalinity. Same color denotes same total emissions.

Additionally, the rain ratio of particulate inorganic carbon to organic carbon is held constant. All of these are likely to vary in the real world.

However, it should also be noted that a robust connection between these changes in the biological pump and climate remains uncertain. For example, today the deep ocean receives water injected from the North Atlantic, which in the modern world has relatively low surface nutrients, and the Southern Ocean, which has relatively high surface nutrients. As noted by Marinov et al. (2008), changes in the balance of deep waters formed in these regions can significantly alter the carbon stored by the biological pump in the deep ocean so that a slowdown in circulation may produce either increased or decreased storage of carbon (with corresponding changes in deep-ocean acidity). While one might expect the total level of vertical exchange to decrease as atmospheric carbon dioxide increases, it is much less clear how the balance between the two source regions would change.

Similarly, there are open questions regarding the rain ratio. While it does seem likely that this value will be a function of carbon saturation state, it is not clear what the dependence should be. While some calcifying organisms like corals (Langdon et al., 2000) and pteropods (Fabry et al., 2008) tend to grow more slowly under higher levels of carbon dioxide, other calcifying organisms such as coccolithophores may become more abundant (S. Rivero-Calle, personal communication, 2014).

See the Supplement for an example of how the scaling laws, which are based on an idealized emission shape, may be used to estimate the peak perturbations from more realistic fossil fuel emission scenarios.
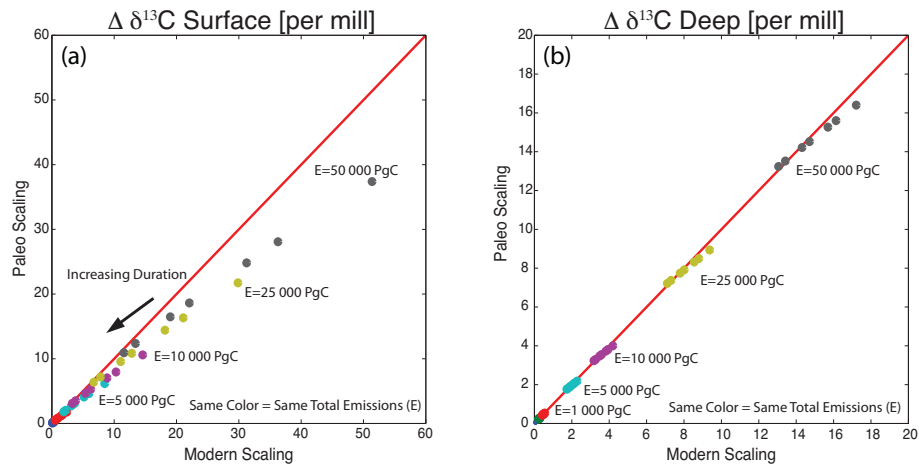
Figure 15. Correlation between peak perturbations for modern and paleo-scalings. **(a)** Surface-ocean carbon-13 anomalies. **(b)** Deep-ocean carbon-13 anomalies. Same color denotes same total emissions.

References

Archer, D., Eby, M., Brovkin, V., Ridgwell, A., Cao, L., Mikolajewicz, U., and Caldeira, K., Matsumoto, K., Munhoven, G., Montenegro, A., and Tokos, K.: Atmospheric lifetime of fossil fuel carbon dioxide, Annu. Rev. Earth Pl. Sc., 37, 117–134, 2009.

Berner, R. A. and Caldeira, K.: The need for mass balance and feedback in the geochemical carbon cycle, Geology, 25, 955–956, 1997.

Berner, R. A. and Kothavala, Z.: GEOCARB III: a revised model of atmospheric CO$_2$ over Phanerozoic time, Am. J. Sci., 301, 182–204, 2001.

Berner, R. A., Lasaga, A. C., and Garrels, R. M.: The carbonate-silicate geochemical cycle and its effect on atmospheric carbon dioxide over the past 100 million years, Am. J. Sci., 283, 641–683, 1983.

Fabry, V. J., Seibel, B. A., Feely, R. A., and Orr, J. C.: Impacts of ocean acidification on marine fauna and ecosystem processes, ICES J. Mar. Sci., 65, 414–432, 2008.

Komar, N. and Zeebe, R. E.: Oceanic calcium changes from enhanced weathering during the Paleocene-Eocene Thermal Maximum: no effect on calcium-based proxies, Paleoceanography, 26, PA3211, doi:10.1029/2010PA001979, 2011.

Komar, N., Zeebe, R. E., and Dickens, G. R.: Understanding long-term carbon cycle trends: the late Paleocene through the early Eocene, Paleoceanography, 28, 650–662, 2013.

Langdon, C., Takahashi, T., Sweeney, C., Chipman, D., and Atkinson, J.: Effect of calcium carbonate saturation on the calcification rate of an experimental coral reef, Global Biogeochem. Cy., 14, 639–654, 2000.

Marinov, I., Gnanadesikan, A., Sarmiento, J. L., Toggweiler, J. R., Follows, M., and Mignone, B. K.: Impact of oceanic circulation on biological carbon storage in the ocean and atmospheric pCO$_2$, Global Biogeochem. Cy., 22, GB3007, doi:10.1029/2007GB002958, 2008.

Matsumoto, K., Sarmiento, J. L., Key, R. M., Aumont, O., Bullister, J. L., Caldeira, K., Campin, J.-M., Doney, S. C., Drange, H., Dutay, J.-C., Follows, M., Gao, Y., Gnanadesikan, A., Gruber, N., Ishida, A., Joos, F., Lindsay, K., Maier-Reimer, E., Marshall, J. C., Matear, R. J., Monfray, P., Mouchet, A., Najjar, R., Plattner, G.-K., Schlitzer, R., Slater, R., Swathi, P. S., Totterdell, I. J., Weirig, M.-F., Yamanaka, Y., Yool, A., and Orr, J. C.: Evaluation of ocean carbon cycle models with data-based metrics, Geophys. Res. Lett., 31, L07303, doi:10.1029/2003GL018970, 2004.

McKay, D. I., Tyrrell, T., Wilson, P. A.,and Foster, G. L.: Estimating the impact of the cryptic degassing of Large Igneous Provinces: A mid-Miocene case-study, Earth Planet. Sci. Lett., 403, 254–262, 2014.

Pälike, H., Lyle, M. W., Nishi, H., Raffi, I., Ridgwell, A., Gamage, K., Klaus, A., Acton, G., Anderson, L., Backman, J., Baldauf, J., Beltran, C., Bohaty, S. M., Bown, P., Busch, W., Channell, J. E. T., Chun, C. O. J., Delaney, M., Dewangan, P., Dunkley, J. T., Edgar, K. M., Evans, H., Fitch, P., Foster, G. L., Gussone, N., Hasegawa, H., Hathorne, E. C., Hayashi, H., Herrle, J. O., Holbourn, A., Hovan, S., Hyeong, K., Iijima, K., Ito, T., Kamikuri, S.-I., Kimoto, K., Kuroda, J., Leon-Rodriguez, L., Malinverno, A., Moore, T. C., Murphy, B. H., Murphy, D. P., Nakamura, H., Ogane, K., Ohneiser, C., Richter, C., Robinson, R., Rohling, E. J., Romero, O., Sawada, K., Scher, H., Schneider, L., Sluijs, A., Takata, H., Tian, J., Tsujimoto, A., Wade, B. S., Westerhold, T., Wilkens, R., Williams, T., Wilson, P. A., Yamamoto, Y., Yamamoto, S., Yamazaki, T., and Zeebe, R. E.: A Cenozoic record of the equatorial Pacific carbonate compensation depth, Nature, 488, 609–614, 2012.

Paquay, F. S. and Zeebe, R. E.: Assessing possible consequences of ocean liming on ocean pH, atmospheric CO$_2$ concentration and associated costs, Int. J. Greenh. Gas Con., 17, 183–188, 2013.

Ridgwell, A. and Hargreaves, J.: Regulation of atmospheric CO_2 by deep-sea sediments in an Earth System Model, Global Biogeochem. Cy., 21, GB2008, doi:10.1029/2006GB002764, 2007.

Ridgwell, A., Hargreaves, J. C., Edwards, N. R., Annan, J. D., Lenton, T. M., Marsh, R., Yool, A., and Watson, A.: Marine geochemical data assimilation in an efficient Earth System Model of global biogeochemical cycling, Biogeosciences, 4, 87–104, doi:10.5194/bg-4-87-2007, 2007.

Sarmiento, J. L. and Gruber, N.: Ocean Biogeochemical Dynamics, Princeton University Press, Princeton, NJ, 2006.

Sarmiento, J. L., Hughes, T. M. C., and Stouffer, R. J.: Simulated response of the ocean carbon cycle to anthropogenic climate warming, Nature, 393, 245–249, 1998.

Sluijs, A., Zeebe, R. E., Bijl, P. K., and Bohaty, S. M.: A middle Eocene carbon cycle conundrum, Nat. Geosci., 6, 429–434, 2013.

Stuecker, M. F. and Zeebe, R. E.: Ocean chemistry and atmospheric CO_2 sensitivity to carbon perturbations throughout the Cenozoic, Geophys. Res. Lett., 37, L03609, doi:10.1029/2009GL041436, 2010.

Tjiputra, J. F., Assmann, K., Bentsen, M., Bethke, I., Otterå, O. H., Sturm, C., and Heinze, C.: Bergen earth system model (BCM-C): model description and regional climate-carbon cycle feedbacks assessment, Geosci. Model Dev., 3, 123–141, doi:10.5194/gmd-3-123-2010, 2010.

Uchikawa, J. and Zeebe, R. E.: Influence of terrestrial weathering on ocean acidification and the next glacial inception, Geophys. Res. Lett., 35, L23608, doi:10.1029/2008GL035963, 2008.

Uchikawa, J. and Zeebe, R. E.: Examining possible effects of seawater pH decline on foraminiferal stable isotopes during the Paleocene-Eocene Thermal Maximum, Paleoceanography, 25, PA2216, doi:10.1029/2009PA001864, 2010.

Walker, J. C. G. and Kasting, J. F.: Effects of fuel and forest conservation on future levels of atmospheric carbon dioxide, Palaeogeography, Palaeoclimatology, Paleoecology, Global Planet. Change, 97, 151–189, 1992.

Walker, J. C. G., Hays, P. B., and Kasting, J. F.: A negative feedback mechanism for the long-term stabilization of Earth's surface temperature, J. Geophys. Res., 86, 9776–9782, 1981.

Zachos, J. C., Röhl, U., Schellenberg, S.,Sluijs, S., Hodell, D. A., Kelly, D. C.,Thomas, E., Nicolo, M., Raffi, I., Lourens, L. J., McCarren, H., and Kroon, D.: Rapid Acidification of the Ocean During the Paleocene-Eocene Thermal Maximum, Science, 308, 1611–1615, 2005.

Zeebe, R. E.: History of seawater carbonate chemistry, atmospheric CO_2, and ocean acidification, Annu. Rev. Earth Pl. Sc., 40, 141–165, 2012a.

Zeebe, R. E.: LOSCAR: Long-term Ocean-atmosphere-Sediment CArbon cycle Reservoir Model v2.0.4, Geosci. Model Dev., 5, 149–166, doi:10.5194/gmd-5-149-2012, 2012b.

Zeebe, R. E. and Zachos, J. C.: Long-term legacy of massive carbon input to the Earth system: Anthropocene vs. Eocene, Philos. T. R. Soc. Lond., 371, 20120006, doi:10.1098/rsta.2012.0006, 2013.

Zeebe, R. E., Zachos, J. C., Caldeira, K., and Tyrrell, T.: Carbon emissions and acidification, Science, 321, 51–52, 2008.

Zeebe, R. E., Zachos, J. C., and Dickens, G. R.: Carbon dioxide forcing alone insufficient to explain Palaeocene-Eocene thermal maximum warming, Nat. Geosci., 2, 576–580, 2009.